2012 IEEE International Conference on Robotics and Automation
RiverCentre, Saint Paul, Minnesota, USA
May 14-18, 2012

Altitude Feedback Control of a Flapping-Wing Microrobot Using an On-Board Biologically Inspired Optical Flow Sensor

Pierre-Emile J. Duhamel, Néstor O. Pérez-Arancibia, Geoffrey L. Barrows, and Robert J. Wood

Abstract— **We present experimental results on the controlled vertical flight of a flapping-wing flying microrobot, in which for the first time an on-board sensing system is used for measuring the microrobot's altitude for feedback control. Both the control strategy and the sensing system are biologically inspired. The control strategy relies on amplitude modulation mediated by optical flow. The research presented here is a key step toward achieving the goal of complete autonomy for flying microrobots, since this demonstrates that strategies for controlling flapping-wing microrobots in vertical flight can rely on optical flow sensors.**

I. INTRODUCTION

Based on the ideas introduced in [1] and [2], a strategy for altitude control of flapping-wing flying 60-mg microrobots of the kind in [3] was presented in [4]. Also, compelling experimental results demonstrating the suitability of the proposed approach were presented. In those cases, the controller design relies on the notion of amplitude modulation of the robot's wing stroke angles and the vertical position of the robot is measured by the use of an external laser position sensor. Here, we present the first controlled vertical flight of a 101-mg flapping-wing microrobot, in which the vertical position fedback into the controller is measured using a biologically-inspired on-board optical flow sensor, similar to the one in [5]. This is a key step toward achieving the goal of complete autonomy for at-scale flying microrobots, since these experimental results unequivocally demonstrate that microrobots of the kind considered here are capable of carrying the extra weight of on-board sensors. More importantly, these results demonstrate that strategies for controlling microrobots in vertical flight can rely on optical flow sensors.

It has been suggested that in natural insects, among all the sensory modalities involved in flight control, visual stimuli are essential for maintaining stability and avoiding obstacles during flight (see [6] and references therein). Also, it is believed that in unidirectional flight, insects use optical flow, defined as the motion of the visual field relative to the eyes, to navigate. Interestingly, it has been known since the 1970s that in most insects, flight has prompted the evolution of the amazing information processing capabilities that we observe in flying insects today [7]. From a robotics perspective, there is evidence that some of the ideas about how insects sense their environment and navigate through it can be applied to generate high-level rules of navigation for ground and flying robotic systems [8].

Inspired by the notion of optical flow, since the late 1990s, visual motion sensors have been developed and applied to a variety of flying prototypes [5], [8]–[18]. For instance, in [17], a 10-g fixed-wing *micro air vehicle* (MAV) capable of regulating airspeed and avoiding lateral collisions was developed, based on a navigation strategy that combines optical flow and gyroscopic information. Another example is the work presented in [8]. There, several navigational strategies based on optical flow employed by bees were described. The feasibility of applying these strategies to robotic systems was tested using unmanned helicopters. Using a 13.6-g flapping-wing MAV, the potentials and limitations of using optical flow on flapping-wing robotic systems was explored in [18]. There, it is argued that periodic oscillations produced by flapping introduce significant bias to the estimates obtained from the measured optical flow.

One of the main contributions presented in this paper is the integration of an optical flow sensor (model Tam4, designed and fabricated by Centeye) with a flapping-wing flying microrobot similar to the one in [3], the *RoboBee*. Furthermore, using modern system identification techniques, a filter is trained for extracting real-time velocity and linear position information from the optical flow measurement. This extracted information is used for controlling the altitude of the flapping-wing microrobot. Total autonomy of *RoboBee*-like MAVs will be achieved by the integration of power, sensing and computational hardware into the robot, which implies the fulfillment of strict mass and size constraints. The results presented here are an important step toward that goal; to the best of our knowledge this is the first empirical demonstration of optical-flow-based control in an at-scale biologically inspired microrobot.

The rest of the paper is organized as follows. Section II describes the flapping-wing microrobot used in the experiments and the main experimental setup. Section III describes the optical flow sensor and the strategy for altitude control. Experimental results are presented in Section IV. Finally, some concluding remarks are given in Section V.

Notation–

- $\mathbb{R}$ and $\mathbb{Z}^+$ denote the sets of real and non-negative integer numbers, respectively.
- The variable t is used to index discrete time, i.e., $t = \{kT_s\}_{k=0}^{\infty}$, with $k \in \mathbb{Z}^+$ and $T_s \in \mathbb{R}$. As usual, T_s is referred to as the sampling-and-hold time.

This work was partially supported by the National Science Foundation (award CCF-0926148) and the Wyss Institute for Biologically Inspired Engineering. P.-E. J. Duhamel is supported by a Graduate Research Fellowship from the National Science Foundation. Any opinions, findings, and conclusions or recommendations expressed in this material are those of the authors and do not necessarily reflect the views of the National Science Foundation.

P.-E. J. Duhamel, N. O. Pérez-Arancibia and R. J. Wood are with the School of Engineering and Applied Sciences, Harvard University, Cambridge, MA 02138, USA, and the Wyss Institute for Biologically Inspired Engineering, Harvard University, Boston, MA 02115, USA (email: pduhamel@fas.harvard.edu; nperez@seas.harvard.edu; rjwood@eecs.harvard.edu). G. L. Barrows is with Centeye Inc., Washington, DC 20008, USA (email: geof@centeye.com).

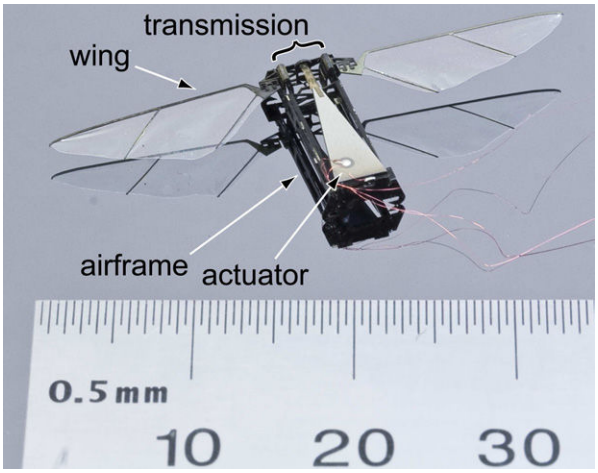

Fig. 1. Photograph of the biologically-inspired two-wing robotic insect, the *RoboBee*.

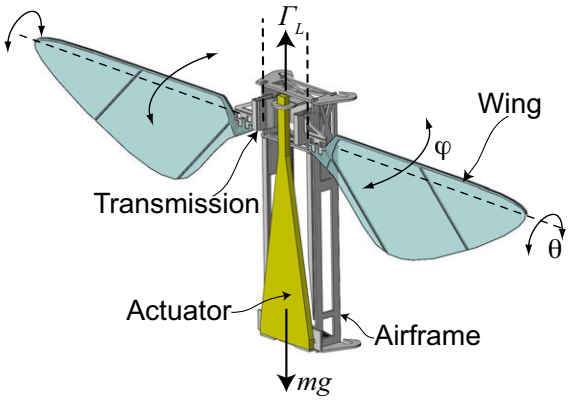

Fig. 2. Illustration of the microrobot employed in the research presented in this article, similar to the one in [3]. This microrobot was entirely designed and fabricated by the authors at the Harvard Microrobotics Laboratory. Γ_L: Average lift force; φ: Flapping angle (also referred to as stroke angle); θ: passive rotation angle.

- The variable τ is used to index continuous time. Thus, for a generic continuous-time variable $x(\tau)$, $x(t)$ is the sampled version of $x(\tau)$.
- z^{-1} denotes the delay operator, i.e., for a signal x, $z^{-1}x(k) = x(k-1)$ and conversely $zx(k) = x(k+1)$. For convenience, z is also the complex variable associated to the z-transform.

II. Description of the Microrobot and Main Experimental Setup

A. Microrobot and Lift Force Generation

The flapping-wing robotic insect used in the experiments is shown in Fig. 1, which was entirely developed and fabricated at the Harvard Microrobotics Laboratory, based upon designs which previously demonstrated the ability to liftoff [3]. The main components include a piezoelectric bending bimorph cantilever actuator [19], a flexure-based transmission, a pair of airfoils, and an airframe which serves as a mechanical ground. The transmission maps the approximately linear motions of the actuator into the flapping motion of the wings. The transmission consists of links and joints with geometries designed to maximize the product of stroke amplitude and first resonant frequency, given known actuator and airfoil properties.

Flight forces are generated through a phenomenon referred to as passive rotation [20]. Here, the wings are connected to the mechanical transmission through flexible hinges, which allow the wings to rotate (angle $\theta(\tau)$ in Fig. 2). This rotation is caused by the inertial forces produced by the flapping $\varphi(\tau)$ and by the aerodynamic forces generated by the interaction of the wings with the air. As explained in [20], an angle θ different than 0° implies that the wings have a positive angle of attack, which causes the generation of lift forces. The microrobot was designed such that, for sinusoidal actuator displacements, drag forces are symmetric about the upstroke and downstroke and the mean lift force vector intersects the center of mass. Thus, ideally, no body torques are generated and the angles of rotation in three dimensions about the robots center of mass (pitch, roll and yaw) should stay at 0°.

In biological literature on flapping-flight [21]–[23], the mean total force, Φ_T, generated by a symmetrical pair of wings throughout the stroke is often estimated as

$$\Phi_T = \int_0^{\Xi} \rho \overline{C}_\Phi \overline{\nu_r^2}(\xi) c(\xi) d\xi, \tag{1}$$

which is a standard quasi-steady blade-element formulation of flight force (see [20] and references therein), where ρ is the density of the air, $\overline{C}_\Phi$ is the mean force coefficient of the wing throughout the stroke, $\overline{\nu_r^2}(\xi)$ is the mean square relative velocity of each wing section, $c(\xi)$ is the chord length of the wing at a distance ξ from the base, and Ξ is the total wing length. In the case of a sinusoidal stroke of frequency f_r, $\varphi(\tau) = \varphi_0 \sin(2\pi f_r \tau)$, with a horizontal stroke plane, the mean square relative velocity of each wing section can be roughly estimated as

$$\begin{aligned} \overline{\nu_r^2}(\xi) &= 4\pi^2 f_r^2 \xi^2 \varphi_0^2 \frac{1}{T_r} \int_0^{T_r} \cos^2(2\pi f_r \tau) d\tau \\ &= 2\pi^2 \xi^2 \varphi_0^2 f_r^2, \end{aligned} \tag{2}$$

with $T_r = f_r^{-1}$. This implies that, regardless of the size and shape of the wing, the estimated mean total flight force is directly dependent on f_r^2 and φ_0^2. This indicates that in order for flying insects to accelerate against gravity or hover at a desired altitude, they can modulate the average lift force by changing the stroke amplitude, φ_0, or by changing the stroke frequency, f_r. For the robots considered here, the transmission that maps the actuator output, labeled as $y(t)$, to the stroke angle $\varphi(t)$ can be approximated by a constant κ_T, i.e., $\varphi(t) = \kappa_T y(t)$. Thus, by changing the amplitude and/or the frequency of $y(t)$, Φ_T can be modulated.

In steady state, the average discrete-time lift force can be estimated as

$$\Gamma_L(t) = \frac{1}{N_L} \sum_{i=0}^{N_L - 1} \gamma_L(t - T_s i), \tag{3}$$

where $\gamma_L(t)$ is the sampled version of the continuous-time instantaneous lift force, $\gamma_L(\tau)$. Here, $t = kT_s$, with fixed $T_s \in \mathbb{R}$ and $0 < N_L \in \mathbb{Z}^+$. Note that assuming steady

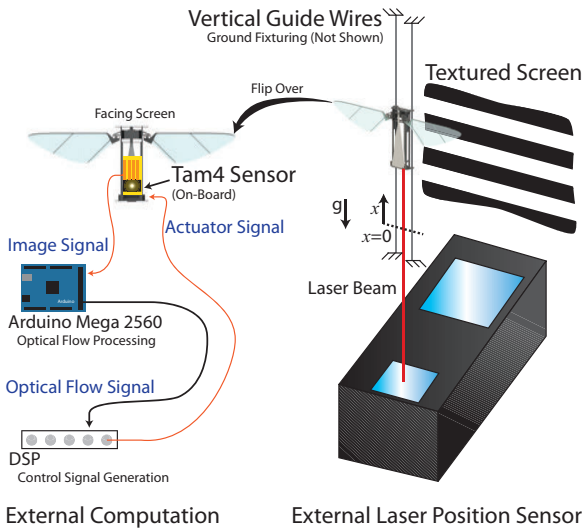

Fig. 3. Setup used in the optical-flow-based altitude control experiments. The altitude x is measured using an on-board Tam4 optical flow sensor and a trained conversion filter. An external laser displacement sensor is used for training the filter that converts optical flow into altitude and for monitoring the position signal estimated by the conversion filter.

state conditions, for the perfectly symmetric flapping case described in the previous paragraph, $\Gamma_L(t)$ can be thought of as an estimate of Φ_T.

From the previous paragraphs it follows that the equation describing the robot's motion along the vertical axis is simply

$$\gamma_L(\tau) - mg = m\ddot{x}(\tau), \tag{4}$$

where m is the mass of the robot and g is the gravitational acceleration constant. As discussed in [1], [2] and [4], the instantaneous lift force $\gamma_L(\tau)$ is a nonlinear function of the frequency and amplitude of the flapping angle φ. Note that for sinusoidal inputs, instantaneous lift forces oscillate around some non-zero mean force, crossing zero periodically. Upward vertical movement occurs when the average lift force, estimated as in (3), is larger than the total robot's weight, mg. Thus, control strategies for hovering and vertical trajectory following can rely on balancing the robot's weight by varying the amplitude of the flapping angle, according to a feedback law. As we will show later, in the experiments presented here, the signal fedback into the controller is optical flow.

B. Main Experimental Setup

The optical-flow-based control experiment is shown in Fig. 3. The experimental setup is a modification of the one described in [4]. There, the vertical position of the microrobot is controlled employing a feedback law that uses a measurement of the altitude x for generating the control signal. In that case, x is measured using a long-range CCD laser displacement sensor LK-2503 fabricated by Keyence. In the research presented here, the altitude x is measured employing a Tam4 on-board optical flow sensor, designed and fabricated by Centeye. Thus, the main contributions of this research are the integration of the Tam4 sensor into the flying microrobot and the use of the optical flow signal for estimating the robot's vertical position, used as feedback for

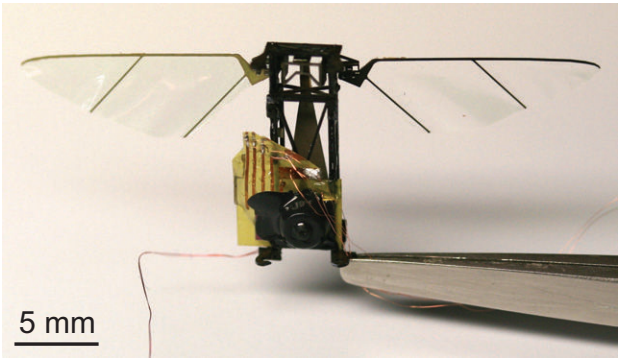

Fig. 4. Integration of the microrobot (*RoboBee*) with the Tam4 image sensor.

real-time altitude control. The integration of the microrobot with the sensing system is shown in Fig. 4. The details about the sensor and the integration process are discussed in the next section.

Optical flow refers to the motion of the visual field relative to the eyes of the obsever. The Tam4 sensor measures optical flow, and thus to increase the signal-to-noise ratio, for this experiment, a textured screen is placed in front of the sensor, as shown in Fig. 3. In this case, the robot's movement is constrained to the vertical degree of freedom using guide wires, and consequently, the optical flow sensor moves in the vertical direction only. As seen in Fig. 3, the image signal captured by the Tam4 sensor is sent to a microprocessor (Arduino Mega 2560), in which a train of pulses proportional to the vertical velocity of the microrobot is generated. The train of pulses, the optical flow signal, is sent to a digital signal processor in which the robot's position information is generated using an identified filter and the control signal input to the piezoelectric actuator is generated. Note that there is not a fundamental reason for using two processors. This is done for experimental convenience and in the final prototype all the signal processing should occur inside a single processor.

III. Optical Flow Sensing and Altitude Control

A. Sensor Hardware and Integration with the Microrobot

The Tam4 image sensor is custom designed for low power and mass applications such as embedded systems and robotics. The sensor chip, shown on the left in Fig. 5-(a), consists of a 4×32 pixel array optimized for sensing motion along a single axis. Pixels on the Tam4 have a $8:1$ aspect ratio (336×42 μm pixel pitch) such that the focal plane is a square with an area of 1.34 mm^2. The pixel electronics uses the typical continuous-time logarithmic-response pixel circuit, allowing for a higher dynamic range of incident radiance to be captured within the output analog voltage range. The logarithmic response mode can also be operated without shuttering, which decreases the weight and complexity of the sensor assembly. The output pixel is selected using a 7 bit counter, with the upper 2 bits selecting the row and the lower 5 bits selecting the column. Incrementing the counter scans out the array pixel-by-pixel row-wise, and sends the resulting pixel signal off-chip as an analog voltage output. The Tam4 chip has on-chip biases. This arrangement allows the chip to

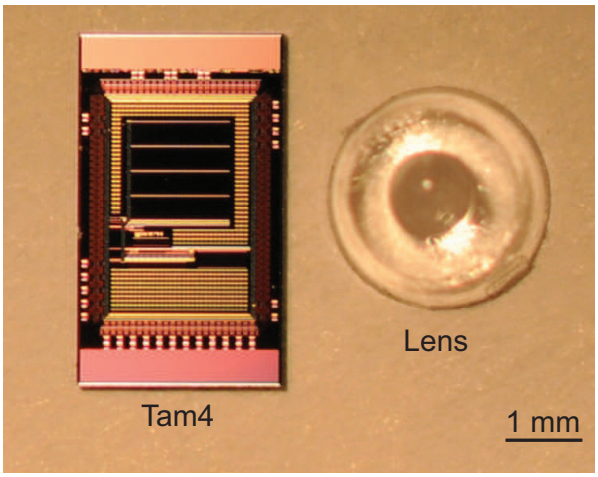

(a)

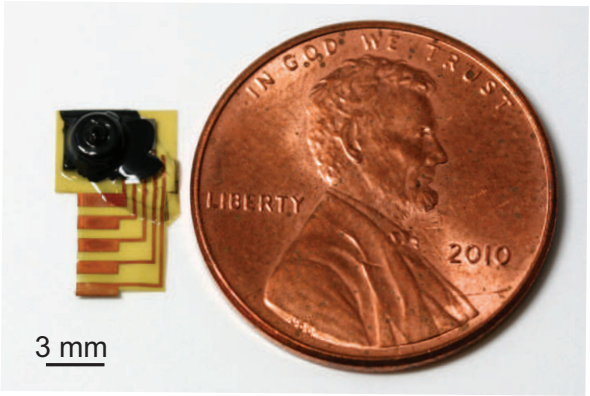

(b)

Fig. 5. (a): Unassembled sensor components, including the Tam4 bare die (left) and acrylic injection-molded lens (right). The Tam4 chip is designed for 1D motion sensing. In its displayed orientation, the Tam4 focal plane is 4 pixels heigh and 32 pixels wide, and would sense motion from left to right. (b): The completed sensor assembly. First, the Tam4 chip is glued and wire bonded to a flex circuit breakout. Then, the injection-molded lens is glued onto the Tam4 focal plane. Lastly, an iris is painted onto the lens surface.

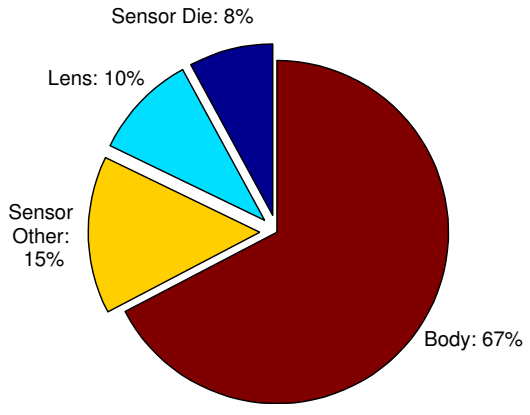

Fig. 6. Breakdown of the *RoboBee* (microrobot + on-board optical flow sensor) mass by component. Total mass of 101 mg. *Sensor other* consists of flex circuit breakout, solder, and glue.

be operated with just five signals: Ground, Power, Increment, Reset, and Output.

In order to create a complete camera, light is focused onto the chip's focal plane using an acrylic injection-molded lens, shown on the right in Fig. 5-(a). This lens is attached directly onto the Tam4 chip using UV curable optically clear adhesive. An iris is formed by covering the lens with black paint except for a hole at the top of the lens. The lens has a focal length just over one millimeter, resulting in a practical field of view of about 70°. When used in the experiments as shown in Fig. 3, the field of view includes approximately four stripes of the textured screen, which results in a sampling of approximately eight pixels per stripe, completely adequate for the purposes of the control experiments discussed here.

When integrating the optical flow sensor into the microrobot, as shown in Fig. 4, many factors are considered simultaneously, such that the resulting microrobotic system maintains its capability of lifting off and maneuver along the vertical axis. All materials and components are made with low mass considerations. A flex circuit breakout, shown in Fig. 5-(b) was designed to interface the bare die Tam4 to the off-board microcontroller used for processing optical flow, resulting in an interface that is significantly lighter than a typical fiberglass printed circuit board (PCB). The backing of the flex circuit was reinforced with s-glass around the Tam4 chip to add a protective ridged backing for the silicon chip and wire bonds with negligible added weight. The Tam4 bare die is glued with conductive epoxy to a ground pad on the flex circuit and necessary signals are wire bonded to 200 μm copper traces. Fine 51 AWG varnished copper wiring between the flex circuit and the optical flow processor, used to transmit the image signal, adds minimal drag as the microrobot ascends along the vertical axis.

The *RoboBee*'s body design is similar to the one used in the altitude control experiments of [4]. However, cross bracing was added to the ventral surface to support mounting of the optical flow sensor to the airframe with cyanoacrylate glue. The final complete microrobotic device, as shown in Fig. 4, has the mass distribution shown in Fig. 6. The *sensor other* category, consisting of the flex circuit, solder, and glue, is currently the greatest mass contribution of the sensor components. The larger copper pads on the flex circuit breakout were primarily used for testing and cut off to decrease mass before final use. There is still room for improvement in decreasing the weights of the various sensor components. For example, the lens mass could be decreased in a future iteration by using printed pinhole optics [24]. In comparison, previous efforts in miniaturization of optical flow sensors described in [25] and applied in [17] combined a 140-mg cut down TSL3301 sensor fabricated by TAOS with 1×102 pixel resolution, a 170-mg lens with case, and a 80-mg PCB for a combined mass of 390 mg. Our 33-mg sensor offers high performance, as seen in Section IV, with approximately $1/10$ the mass, by using less packaging, lighter optics, and thinner circuitry.

As depicted in Fig. 3, the Tam4 image sensor interfaces with the off-board Arduino Mega 2560 microcontroller, which captures images and computes optical flow. Optical flow is computed using a modified version of the *Image Interpolation Algorithm* (IIA) [26]. Since the Tam4 sensor

is a 1D sensor with a high aspect ratio array of pixels, optical flow is only calculated and communicated for the 1D long axis of the image sensor. To further simplify the optical flow calculations, only a single 1×32 pixel column from the captured images is used in the calculation of the 1D optical flow signal. The optical flow signal is input to control algorithms that are computed by an off-board DSP; communication of the optical flow signal was completed using an RS-232 serial connection at 9600 Bd. The pulses composing the optical flow train are received at a non-constant rate of approximately 40.5 Hz. A buffering strategy in the communication between the two processors in Fig. 3 ensures that no data is lost in the transmission process.

B. Control Strategy

In [1], [2] and [4], it was shown that the dynamics of the microrobot in Fig. 1 can be modeled as

$$y(t) = [Pu](t) + d(t), \tag{5}$$

where P is a linear time-invariant (LTI) system, $u(t)$ is the input voltage driving the piezoelectric actuator, $y(t)$ is the displacement of the distal end of the actuator, and $d(t)$ is the output disturbance representing the aggregated effects of all the disturbances affecting the system, including vibrations generated by the aerodynamic forces produced by the wing flapping. In [1], [2] and [4], it was also shown that using modern LTI system identification techniques, a model of P, $\hat{P}$, can be found. Using $\hat{P}$, an adaptive strategy can be designed and implemented to force the actuator displacement $y(t)$ to follow desired references with the form $y_d(t) = A_d \sin(2\pi f_d t)$.

As explained in [4], static experiments, in which the actuator displacement $y(t)$ and the instantaneous lift force $\gamma_L(t)$ are measured simultaneously, can be performed in order to find relationships between actuator displacements and generated lift forces. This is relevant, because as mentioned in Section II, the relationship between $y(t)$ and $\varphi(t)$ can be modeled as $\varphi(t) = \kappa_T y(t)$, with κ_T constant. The measurement of $y(t)$ is done using a short-range CCD laser displacement sensor LK-2001 fabricated by Keyence. The instantaneous force $\gamma_L(t)$ is measured by sensing the deflection of a double-cantilever beam to which the microrobot is rigidly connected. The beam deflection is measured using a capacitive displacement sensor (for details on the force sensor design see [27]). Thus, using the adaptive control strategy in [2], the data in Fig. 7 was generated. This plot shows experimental cases in which for actuator displacements with the form $y(t) = A \sin(2\pi f t)$, the frequency f is fixed and the amplitude A is varied in order to obtain an empirical relationship between the amplitude and the average lift force $\Gamma_L(t)$. The information in Fig. 7 is crucial when choosing the parameters of the laws for controlling altitude.

As commented in Section II, the average lift force $\Gamma_L(t)$ can be modulated by varying the frequency or amplitude of the flapping angle φ, assuming that this follows a sinusoidal trajectory as it is commonly observed in nature and in man-made flapping-wing machines. As in [4], in the experiments presented here, we use amplitude modulation, i.e., we fix the frequency of flapping and vary the amplitude. Formally, the input signals to the piezoelectric actuator have the form

$$u(t) = a_u(t) \sin(2\pi f_u t). \tag{6}$$

The idea is to think of $\sin(2\pi f_u t)$ as a part of the system, as shown in Fig. 8, and consider $a_u(t)$ to be the control signal, generated according to some control law. This notion is illustrated in Fig. 9. Thus, in closed loop, the signal applied to the system in Fig. 9 has the form

$$a_u(t) = \begin{cases} \overline{a_u} & \text{if } b_u(t) \geq \overline{a_u} \\ b_u(t) & \text{if } \underline{a_u} < b_u(t) < \overline{a_u} \\ \underline{a_u} & \text{if } b_u(t) \leq \underline{a_u} \end{cases} \tag{7}$$

with

$$b_u(t) = K(z) e_x(t), \tag{8}$$

where $K(z)$ is a discrete-time LTI operator depending on the delay operator z^{-1}. The real numbers $\underline{a_u}$ and $\overline{a_u} \in [0, 1]$ are the minimum and maximum allowable values that $a_u(t)$ can take. The signal $e_x(t)$ is the control error defined as $e_x(t) = x_d(t) - x(t)$, where $x_d(t)$ is the desired altitude and, as stated before, $x(t)$ is the optical-flow-based measured altitude signal, as depicted in Fig. 3.

As proposed in [4], a model of the plant G in Fig. 9 can be found using modern system identification techniques. In this case, the system identification of G is extremely challenging from an experimental point of view. Here, using the experimental technique introduced in [4], a model of G, for the case $f_u = 110$ Hz, was computed. Using this identified model and classical controller design techniques, an LTI operator $K(z)$ for the law in (8) was found and evaluated, employing the classical gain and phase margin indices.

Now, we look at the information contained in Fig. 7 to justify the choice of $f_u = 110$ Hz and choose the parameters $\overline{a_u}$ and $\underline{a_u}$ for the nonlinear control law in (7). In Fig. 7, for all the frequencies considered (70, 80, 90, 100 and 110 Hz), $A = 1$ means that the amplitude of $y(t)$ is equal to the constant displacement of the actuator when the system P is excited with a constant $u(t) = 1$. Also, $u(t) = 1$ means that the actuator is excited at its maximum allowable voltage, 300 V. Thus, considering that the microrobot used here has a mass of 101 mg, in the experiment presented in Section IV, the chosen fixed frequency is $f_u = 110$ Hz and the upper bound $\overline{a_u}$ is 0.8, which give one a comfortable margin of robustness with respect to variations in the average lift-force generated by the robot. This follows from noting in Fig. 7 that for $f_u = 110$ Hz, with $\overline{a_u} = 0.8$, there exists a significant margin between the force required for hovering (101 mg) and the average lift forces generated by the robot.

IV. Experimental Results

A. Conversion of Optical Flow to Altitude

First in this section, we discuss the conversion from optical flow to altitude. The objective here is to find a dynamic mapping from the optical flow signal $o(t)$ to the altitude $x(t)$, Ψ. In order to do this, we use the measurement of the altitude obtained with the external long-range laser displacement sensor as shown in Fig. 3. In this subsection, we call this signal $x_s(t)$, to distinguish from $x(t)$, which is the measurement that results from processing the optical

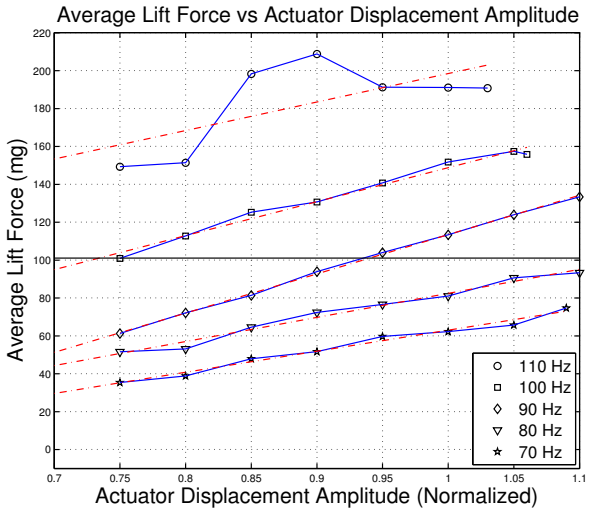

Fig. 7. Empirical relationship between average lift force, $\Gamma_L(t)$, and actuator displacement, $y(t) = A\sin(2\pi ft) \approx y_d(t) = A_d\sin(2\pi f_d t)$, with a fixed frequency f_d taking the values of 70, 80, 90, 100 and 110. Hz. Here, A is normalized so that a unit input to $P(z)$, $u(1) = 1$, produces a unit output $y(t) = 1$. Also, $u(t) = 1$ means that the actuator is excited at its maximum allowable voltage, 300 V. Each data point was computed from $200,000$ samples, obtained at 10 KHz. The thicker black horizontal line marks the liftoff threshold for the *RoboBee* considered in this case.

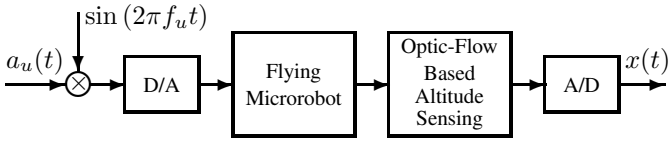

Fig. 8. Block diagram of the integrated microrobot with on-board sensing system, used in the altitude control experiments. Note that the altitude $x(t)$ is measured using an optical-flow-based sensing system.

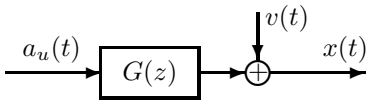

Fig. 9. Idealized system dynamics. $G(z)$: Discrete-time open-loop plant; $a_u(t)$: Input amplitude; $x(t)$: Measured altitude; $v(t)$: Output disturbance, representing the aggregated effects of all the disturbances affecting the system, including stochastic wind currents. $G(z)$ is idealized under the assumption that the frequency f_u is fixed and that $a_u(t)$ oscillates around a_H, which is the exact amplitude required for hovering.

flow signal $o(t)$. Note that for convenience $o(t)$ is treated as a 10 KHz signal formed by zeros and spikes that contain the optical flow information. In the upper plot of Fig. 10, a sequence of the altitude $x_s(t)$, sampled at 10 KHz, is shown. The bottom plot in Fig. 10 shows the corresponding optical flow train of pulses (spaced at a non-constant frequency about 40.5 Hz), whose magnitude is proportional to velocity. This specific signal $x_s(t)$ is high frequency compared to the dynamics of the microrobot in vertical flight. Thus, this signal can be used to estimate the mapping Ψ from the data.

Two simple methods are proposed for representing Ψ. These are illustrated in Fig. 11. The first method uses the LTI filter F_1 and yields $x_1(t)$; the second uses the LTI filter F_2 and yields $x_2(t)$. Everything else is the same. The Value

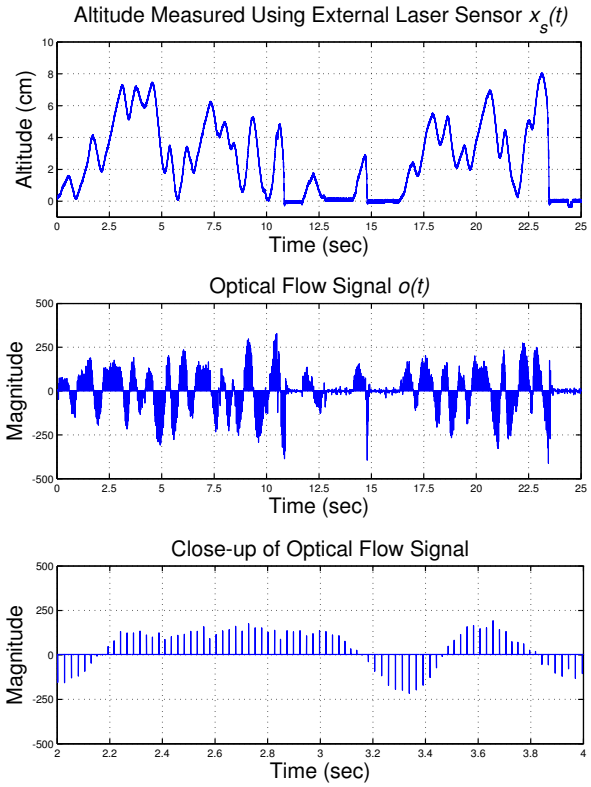

Fig. 10. Experimental data used for estimating the operator Ψ that maps the optical flow signal, $o(t)$, to altitude, $x(t)$, i.e., $x = \Psi o$. *Upper Plot:* Altitude measured using external laser sensor, $x_s(t)$. *Middle Plot:* Optical Flow Signal $o(t)$. *Bottom Plot:* Close-up of optical flow signal $o(t)$.

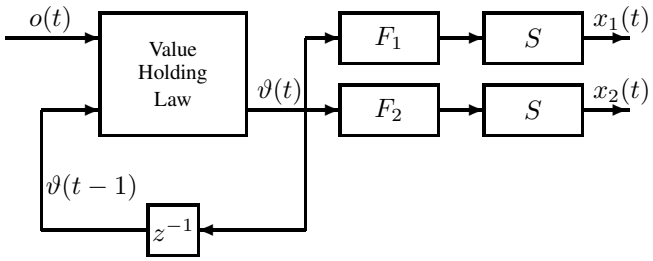

Fig. 11. Block diagram of the two methods proposed for mapping the optical flow signal, $o(t)$, to altitude, $x(t)$, i.e., finding an operator Ψ so that $x(t) = [\Psi o](t)$. The filter F_1 is estimated using the $n4sid$ subspace system identification method [28]. The filter F_2 is a simple discrete-time integrator. The operator S saturates the signal so that the estimate $x(t)$ is always positive.

Holding Law is defined as

$$\vartheta(t) = \begin{cases} \vartheta(t-1) & \text{if } o(t) = 0 \\ o(t) & \text{otherwise} \end{cases} \tag{9}$$

where $\vartheta(t)$ is the input to the LTI filters $F_1(z)$ and $F_2(z)$, as shown in Fig. 11. Here, $F_1(z)$ is identified using the subspace state-space $n4sid$ algorithm in Matlab [28], using the data in Fig. 10, assuming that ϑ is the input and $x_s(t)$ is the output. The method yields a 48th-order discrete-time state-space realization, which is reduced to a 2nd-order representation, using balanced reduction techniques [29], [30]. The resulting

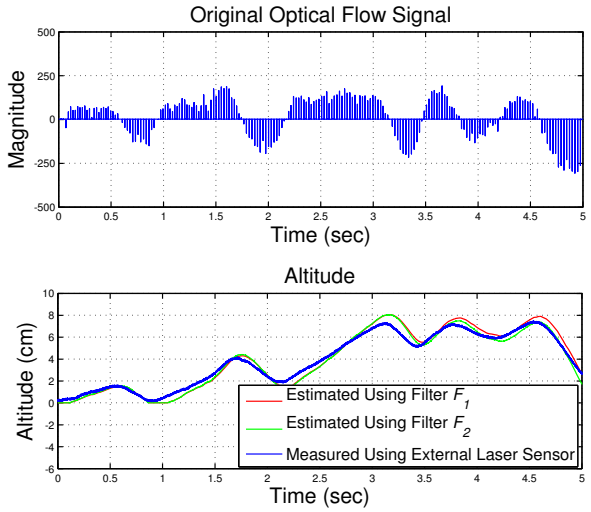

Fig. 12. Example showing the use of both proposed methods in Fig. 11 for mapping the optical flow signal, $o(t)$, to altitude, $x(t)$. *Upper Plot:* Original optical flow signal. *Bottom Plot:* Measured altitude, using filter F_1 (red), filter F_2 (green) and the external laser displacement sensor in Fig. 3 (blue).

approximated state-space representation matrices are

$$A_{F_1} = \begin{bmatrix} 0.99999 & 0.00007 \\ 0.00007 & -0.73670 \end{bmatrix}, \; B_{F_1} = \begin{bmatrix} -0.00092 \\ 0.00590 \end{bmatrix},$$

$$C_{F_1} = \begin{bmatrix} -0.00001 & 0.00007 \end{bmatrix}, \; D_{F_1} = 0.00000.$$

The filter $F_2(z)$ is simply a discrete-time integrator with the form

$$F_2(z) = K_I \frac{z+1}{z-1}, \tag{10}$$

with $K_I = 1.47404 \times 10^{-4}$. The idea of using an integrator comes from noting that the spikes in $o(t)$ are proportional to velocity. Additionally, the low-pass shape of $F_1(z)$ indicates that any tuned low-pass filter might be suitable for the task considered here. The last element to describe in Fig. 11 is the operator S, which is a saturation with the form

$$x(t) = \begin{cases} 0 & \text{if } [F\vartheta](t) \leqslant 0 \\ [F\vartheta](t) & \text{otherwise.} \end{cases} \tag{11}$$

An example illustrating the use of both methods is shown in Fig. 12. According to several trials, it was found that the use of F_1 yields slightly better results than the use of F_2. For this reason, for the flight experiments presented in the next section we used F_1 to estimate the altitude $x(t)$ from the optical flow signal $o(t)$.

B. Flight Experiments

In this subsection, we show an experimental case demonstrating the use of the on-board optical flow sensor for controlling altitude. The results are summarized in Fig. 13 and Fig. 14. The objective is to make the microrobot reach a desired vertical position (5 cm) and hover at that position until $Time = 20$ s. As can be seen in Fig. 13, the robot starts flapping at $Time = 1$ s, with a fixed $a_u(t) = \frac{1}{3}$. Then, at $Time = 5$ s, the control loop is closed and the control signal $a_u(t)$ immediately reaches its maximum allowable

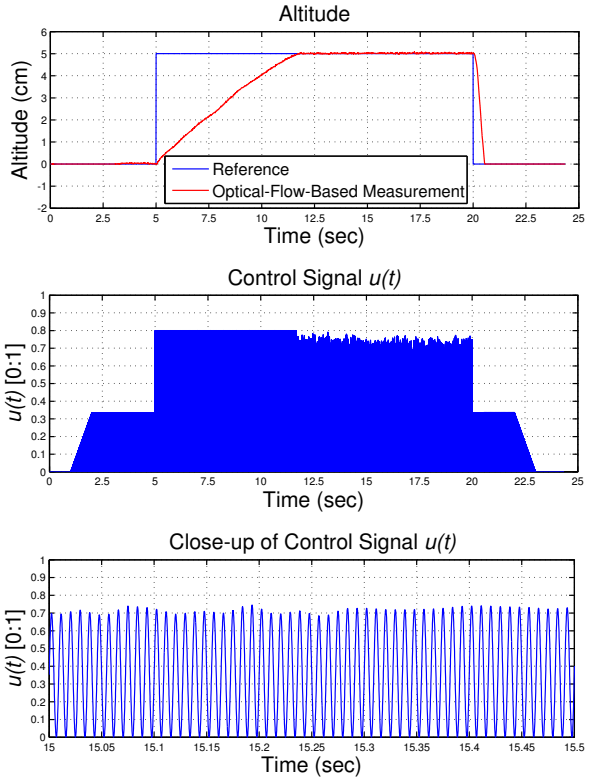

Fig. 13. Hovering experiment. *Upper Plot:* Optical-flow-based altitude measurement $x(t)$ and reference $x_d(t)$. *Middle Plot:* Control signal $u(t) = a_u(t)\sin(2\pi f_u t)$, with $\underline{a_u} = \frac{1}{3}$, $\overline{a_u} = 0.8$ and $f_u = 110$ Hz. *Bottom Plot:* Close-up of the control signal $u(t)$.

value $\overline{a_u} = 0.8$ and stays at that value until the *RoboBee* reaches the desired altitude of 5 cm. While hovering at 5 cm, the controller compensates for disturbances by varying the value of $a_u(t)$, as shown in the middle plot in Fig. 13. Frames from a video sequence showing the transition of the robot from 0 cm to 5 cm and hovering are shown in Fig. 14.

Although the controller performance is excellent when the *RoboBee* is hovering, according to the measured signals, from the video sequence in Fig. 14 it can be seen that small oscillations and a slow, almost imperceptible, drift upwards affects the microrobot. This small discrepancy can be explained by the existence of sensing noise, which implies that the design of the mapping filter can be further improved. The complete experiment is shown in the supplemental movie S1 available at [31]. Note, that the quality of the experimental results presented here is comparable to those in [4], obtained with the use of an external, bulky laser sensor. This is compelling evidence that the use of on-board optical flow sensors is a key step toward the goal of creating completely autonomous *RoboBees*.

V. Conclusion

In this article, we presented experimental results on the first controlled vertical flight of a 101-mg flapping-wing microrobot, in which the altitude was measured using an on-board optical flow sensor. During the development of this research many challenges were overcome, including the fabrication and integration of on-board sensing capabilities into the microrobot, while meeting the strict low mass and

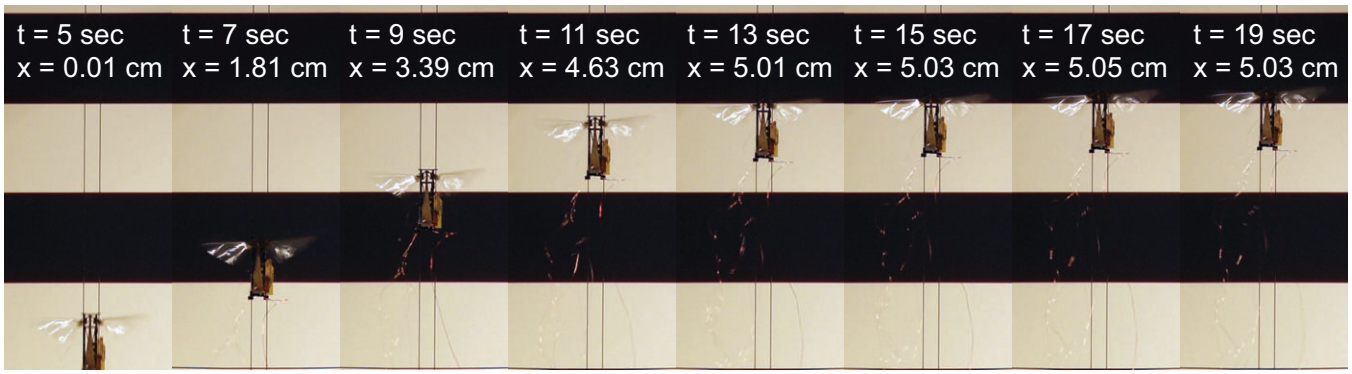

Fig. 14. Video sequence showing the transition from 0 cm to 5 cm and hovering corresponding to the experiment in Fig. 13. The vertical position, $x(t)$, of the microrobot is measured using an on-board optical-flow-based sensor. A movie of the entire experiment is shown in the supplemental movie S1 available at [31].

small size requirements for liftoff. Also, this paper described the design and implementation of real-time controllers and signal processing algorithms required for the fusion of on-board sensing with the microrobot. The achieved control performance with the on-board sensor is comparable to the one in [4], where an external laser displacement sensor was used for measuring altitude. The research presented here is a key step toward achieving the goal of complete autonomy for flying microrobots.

REFERENCES

[1] N. O. Pérez-Arancibia, J. P. Whitney, and R. J. Wood, "Lift Force Control of a Flapping-Wing Microrobot," in *Proc. 2011 Amer. Cont. Conf.*, San Francisco, CA, Jul. 2011, pp. 4761–4768.

[2] N. O. Pérez-Arancibia, J. P. Whitney, and R. J. Wood, "Lift Force Control of Flapping-Wing Microrobots Using Adaptive Feedforward Schemes," to appear in *IEEE/ASME Trans. Mechatron.*, 2011.

[3] R. J. Wood, "The First Takeoff of a Biologically Inspired At-Scale Robotic Insect," *IEEE Trans. Robot.*, vol. 24, no. 2, pp. 341–347, Apr. 2008.

[4] N. O. Pérez-Arancibia, K. Y. Ma, K. C. Galloway, J. D. Greenberg, and R. J. Wood, "First Controlled Vertical Flight of a Biologically Inspired Microrobot," *Bioinspir. Biomim.*, vol. 6, no. 3, pp. 036 009–1–11, Sept. 2011.

[5] W. E. Green, P. Y. Oh, and G. Barrows, "Flying Insect Inspired Vision for Autonomous Aerial Robot Maneuvers in Near-Earth Enviroments," in *Proc. Int. Conf. Robot. Autom.*, New Orleans, LA, Apr. 2004, pp. 2347–2352.

[6] R. Dudley, *The Biomechanics of Insect Flight*. Princeton, NJ: Princeton University Press, 2000.

[7] D. Burkhardt, "On the vision of insects," *J. Comp. Physiol. A*, vol. 120, no. 1, pp. 33–50, Jan. 1977.

[8] M. V. Srinivasan, S. W. Zhang, J. S. Chahl, G. Stange, and M. Garratt, "An overview of insect-inspired guidance for application in ground and airborne platforms," *Proc. Inst. Mech. Eng., G: J. Aerosp. Eng.*, vol. 218, no. 6, pp. 375–388, June 2004.

[9] G. L. Barrows, *MIxed-Mode VLSI Optic Flow Sensors for Micro Air Vehicles*. College Park, MD: Ph.D. Dissertation, University of Maryland, College Park, 1999.

[10] G. L. Barrows, K. T. Miller, and B. Krantz, "Fusing Neuromorphic Motion Detector Outputs for Robust Optic Flow Measurement," in *Proc. Int. Joint Conf. Neural Netw.*, Washington, DC, Jul. 1999, pp. 2296–2301.

[11] G. L. Barrows and C. Neely, "Mixed-Mode VLSI Optic Flow Sensors for In-Flight Control of a Micro Air Vehicle," in *Proc. SPIE 4109, 52*, San Diego, CA, Jul. 2000.

[12] G. L. Barrows, J. S. Chahl, and M. V. Srinivasan, "Biomimetic Inspired Visual Sensing and Flight Control," *Aeronaut. J.*, vol. 107, no. 1069, pp. 159–168, Mar. 2003.

[13] F. Ruffier, S. Viollet, S. Amic, and N. Franceschini, "Bio-Inspired Optical Flow Circuits for the Visual Guidance of Micro-Air Vehicles," in *Proc. IEEE Int. Symp. Circuits Syst.*, Bangkok, Thailand, May 2003, pp. 846–849.

[14] W.-C. Wu, L. Schenato, R. J. Wood, and R. S. Fearing, "Biomimetic Sensor Suite for Flight Control of a Micromechanical Flying Insect: Design and Experimental Results," in *Proc. IEEE Int. Conf. Robot. Autom.*, Taipei, Taiwan, Sep. 2003, pp. 1146–1151.

[15] F. Ruffier and N. Franceschini, "Optic flow regulation: the key to aircraft automatic guidance," *Robot. Autom. Syst.*, vol. 50, no. 4, pp. 177–194, Mar. 2005.

[16] R. J. Wood, S. Avadhanula, E. Steltz, M. Seeman, J. Entwistle, A. Bachrach, G. Barrows, S. Sanders, and R. S. Fearing, "An Autonomous Palm-Sized Gliding Micro Air Vehicle," *IEEE Robot. Autom. Mag.*, vol. 14, no. 2, pp. 82–91, June 2007.

[17] J.-C. Zufferey, A. Klaptocz, A. Beyeler, J.-D. Nicoud, and D. Floreano, "A 10-gram vision-based flying robot," *Proc. Inst. Mech. Eng., G: J. Aerosp. Eng.*, vol. 21, no. 14, pp. 1671–1684, Dec. 2007.

[18] F. Garcia Bermudez and R. Fearing, "Optical Flow on a Flapping Wing Robot," in *Proc. IEEE/RSJ Int. Conf. Intell. Robot. Syst.*, St. Louis, MO, Oct. 2009, pp. 5027–5032.

[19] R. J. Wood, E. Steltz, and R. S. Fearing, "Nonlinear Performance Limits for High Energy Density Piezoelectric Bending Actuators," in *Proc. IEEE Int. Conf. Robot. Autom.*, Barcelona, Spain, Apr. 2005, pp. 3633–3640.

[20] J. P. Whitney and R. J. Wood, "Aeromechanics of passive rotation in flapping flight," *J. Fluid Mech.*, vol. 660, pp. 197–220, Oct. 2010.

[21] F.-O. Lehmann and M. H. Dickinson, "The Control of Wing Kinematics and Flight Forces in Fruit Flies (Drosophila spp.)," *J. Exp. Biol.*, vol. 201, no. 3, pp. 385–401, Feb. 1998.

[22] C. P. Ellington, "The Aerodynamics of Hovering Insect Flight. VI. Lift and Power Requirements," *Phil. Trans. R. Soc. Lond. B*, vol. 305, no. 1122, pp. 145–185, Feb. 1984.

[23] T. Weis-Fogh, "Quick Estimates of Flight Fitness in Hovering Animals, Including Novel Mechanisms for Lift Production," *J. Exp. Biol.*, vol. 59, no. 1, pp. 169–230, Aug. 1973.

[24] G. Barrows, "Low profile camera and vision sensor," US Patent Application No. US 12/710073., Publication No. US 2011/0026141, February 2011.

[25] A. Klaptocz, *Miniature Cameras for Ultra-Light Flying Robots*. Lausanne, Switzerland: E&CE Fourth Year Design Project, University of Waterloo and Ecole Polytechnique Fédérale de Lausanne, 2005.

[26] M. V. Srinivasan, "An image-interpolation technique for the computation of optic flow and egomotion," *Biol. Cybern.*, vol. 71, no. 5, pp. 401–415, Sept. 1994.

[27] R. J. Wood, K.-J. Cho, and K. Hoffman, "A novel multi-axis force sensor for microrobotics applications," *Smart Mater. Struct.*, vol. 18, no. 12, pp. 125 002–1–7, Dec. 2009.

[28] P. Van Overschee and B. De Moor, *Subspace Identification for Linear Systems*. Boston, MA: Kluwer, 1996.

[29] A. J. Laub, M. T. Heath, C. C. Paige, and R. C. Ward, "Computation of System Balancing Transformations and Other Applications of Simultaneous Diagonalization Algorithms," *IEEE Trans. Autom. Control*, vol. 32, no. 2, pp. 115–122, Feb. 1987.

[30] G. E. Dullerud and F. Paganini, *A Course in Robust Control Theory*. New York, NY: Springer-Verlag, 2000.

[31] P.-E. J. Duhamel, N. O. Pérez-Arancibia, G. L. Barrows, and R. J. Wood, "S1," *http://micro.seas.harvard.edu/ICRA2012/S1.mp4*, Oct. 2011.